J. Fluid Mech. (1989), *vol.* 202, *pp.* 263–294
Printed in Great Britain

Reynolds stress development in pressure-driven three-dimensional turbulent boundary layers

By SHAWN D. ANDERSON† AND JOHN K. EATON
Department of Mechanical Engineering, Stanford University, Stanford, CA 94305, USA

(Received 25 November 1987 and in revised form 23 July 1988)

The development of the Reynolds stress field was studied for flows in which an initially two-dimensional boundary layer was skewed sideways by a spanwise pressure gradient ahead of an upstream-facing wedge. Two different wedges were used, providing a variation in the boundary-layer skewing. Measurements of all components of the Reynolds stress tensor and all ten triple products were measured using a rotatable cross-wire anemometer. The results show the expected lag of the shear stress vector behind the strain rate. Comparison of the two present experiments with previous data suggests that the lag can be estimated if the radius of curvature of the free-stream streamline is known. The magnitude of the shear stress vector in the plane of the wall is seen to decrease rapidly as the boundary-layer skewing increases. The amount of decrease is apparently related to the skewing angle between the wall and the free stream. The triple products evolve rapidly and profiles in the three-dimensional boundary layer are considerably different than two-dimensional profiles, leaving little hope for gradient transport models for the Reynolds stresses. The simplified model presented by Rotta (1979) performs reasonably well providing that an appropriate value of the T-parameter is chosen.

1. Introduction

Three-dimensional turbulent boundary layers in which there are significant normal gradients of both the streamwise and spanwise velocity components are much more common in practice than the classical two-dimensional boundary layer. A simple but commonly occurring three-dimensional one is an initially two-dimensional boundary layer which is deflected by a spanwise pressure gradient. The low-momentum flow adjacent to the wall is deflected to a greater angle than is the free stream, resulting in the characteristic velocity profiles shown in figure 1.

For moderate pressure gradients, the three-dimensional boundary layer remains attached and the streamwise and spanwise vorticity components are dominated by $\mathrm{d}W/\mathrm{d}y$ and $\mathrm{d}U/\mathrm{d}y$ respectively. (We shall use the convention that x, y, z are the streamwise, normal and spanwise directions, respectively. The associated velocity components are u, v and w. Capital letters refer to time-averaged quantiies and primes refer to fluctuating quantities. The coordinate system is fixed relative to the laboratory and the initially two-dimensional layer.) The primary function of a turbulence model in such flows is to predict the magnitude and direction of the shear stress vector in planes parallel to the wall. This vector (subsequently called 'shear stress vector'), which is composed of the $\overline{u'v'}$ and $\overline{v'w'}$ shear stress components, governs the boundary-layer development. Most current computational methods

† Present address: Shell Development Corporation, Houston, Texas.

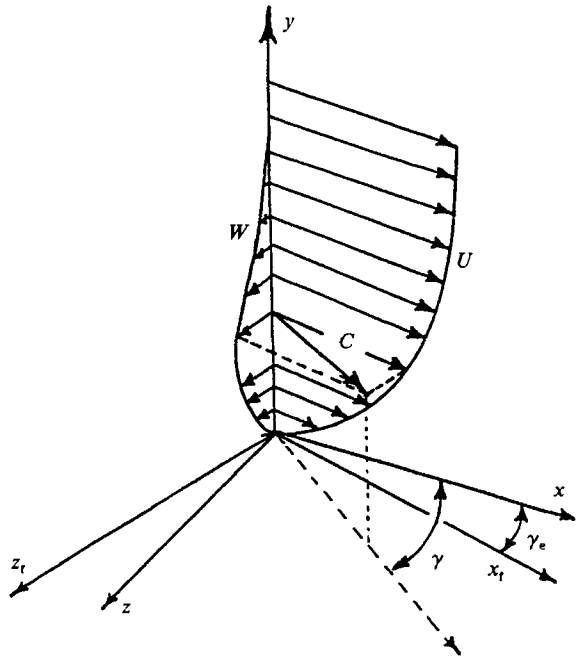

FIGURE 1. Characteristic velocity profile shape of a pressure-driven three-dimensional boundary layer.

assume an isotropic eddy viscosity and use slightly modified two-dimensional models to predict the eddy viscosity. Such assumptions are not in accord with the data, which show that the shear stress vector is rarely aligned with the strain rate. Some recent work following Rotta (1979) has attempted to remedy this with only partial success (see the more complete discussion below).

One of the problems in developing models for three-dimensional turbulent boundary layers is that the turbulence may be strongly distorted by the extra strain rate dW/dy. For example, Bradshaw & Pontikos (1985) found that the ratio of shear stress magnitude to turbulent kinetic energy in a three-dimensional boundary layer fell to around one half of the value typical of two-dimensional boundary layers. There are at least three effects responsible for changing the turbulence structure. First, the additional strain rate dW/dy distorts the existing turbulence structure. Secondly, new production terms appear in the Reynolds stress transport equations when the extra strain rate is applied. Finally, the boundary conditions are changing. For example, in a flow which is turning monotonically, the skin friction vector rotates continuously.

Townsend (1980) (see also Savill 1987) suggested that modifications to shear-flow turbulence by extra strain rates can be predicted using rapid distortion theory, reasoning that the extra production terms are usually insignificant. The available data indicate that the distortion of the turbulence structure is indeed an important effect. However, the distortions applied in most three-dimensional turbulent boundary layers are not truly rapid and both the second and third effects mentioned above may be important.

The fact that the directions of the shear stress and strain rate vectors differ substantially in three-dimensional turbulent boundary layers suggests that a turbulence model based on the Reynolds stress transport equations is needed.

However, the distortion of the turbulence by the extra strain rate would appear in the pressure–rate-of-strain correlation. This term in the equations is not measurable at present, so, modellers will have little support from experiments.

Relatively simple models for the shear stress magnitude and direction are needed. The development of such models will require more experimental data than currently exists. Data are needed that show the development of the shear stress vector over a wide range of conditions. There are relatively few good data sets available, largely owing to the difficulties encountered in measuring all components of the Reynolds stress tensor, particularly the $\overline{v'w'}$ shear stress. Hot-wire techniques for the measurement of shear stresses require considerable care. Most investigators have used cross-wire anemometers which require a subtraction of two large numbers to obtain the relatively small $\overline{v'w'}$ stress. Triple-wire techniques are under development (Moffatt, Yavuzkurt & Crawford 1979; Muller 1987) but successful measurements of the full stress tensor are yet to be demonstrated. Accurate measurement of the shear stresses, particularly $\overline{v'w'}$ has proved to be very difficult using laser Doppler anemometer (LDA) techniques in air flow facilities (Driver & Hebbar 1985). Pulsed-wire techniques for measurement of the full stress tensor have only recently been developed (Castro & Cheun 1982) and pulsed-wire probes usually do not have sufficient resolution for attached-boundary-layer studies.

An extensive review of previous experimental studies of subsonic three-dimensional turbulent boundary layers is contained in Anderson & Eaton (1987). Relatively few data sets contain the detailed and accurate Reynolds stress data needed for model development. The simplest experiments are the 'infinite swept wing' experiments of van den Berg, Elsenaar & Lindhout (1975) and Bradshaw & Pontikos (1985). The shear stress vector was found to lag behind the strain rate vector and the aforementioned drop in the shear stress/kinetic energy ratio was observed. Johnston (1970) examining an infinite swept forward-facing step flow observed a dramatic lag of the shear vector. Johnston's general conclusions were supported by the later work of East & Sawyer (1979).

Experiments in somewhat more complicated geometries have arrived at different conclusions. For example, Ezekwe Pierce & McAllister (1978), Fernholz & Vagt (1981), and Muller (1982) have all observed a lead in the shear stress vector ahead of the strain rate. Fernholz & Vagt (1981) concluded that this was caused by very rapid distortions of the turbulence. Van den Berg (1982) observed, though, that this lead only appeared in boundary layers approaching separation.

Variation of the experimental parameters using a fixed facility and measurement techniques will be very useful for understanding which system parameters control the development of the Reynolds stresses. All of the experiments mentioned above are single-configuration experiments, that is there has been no variation of the experimental parameters. The lone exception is a series of experiments conducted by Professor Bradshaw's group at Imperial College on infinite-swept-wing flows with varying longitudinal curvature (Bradshaw & Pontikos 1985; Baskaran & Bradshaw 1987*a*). They found that many of the most important effects of mean flow three-dimensionality were unchanged by longitudinal curvature.

The objective of the present set of experiments was to examine the development of the Reynolds stresses in an initially two-dimensional boundary layer driven to three-dimensionality by a spanwise pressure gradient. A single-parameter experiment was desired in which the ratio of the spanwise to the streamwise pressure gradient could be varied. This objective was partially met using the geometry sketched in figure 2. A two-dimensional boundary layer is deflected sideways by the

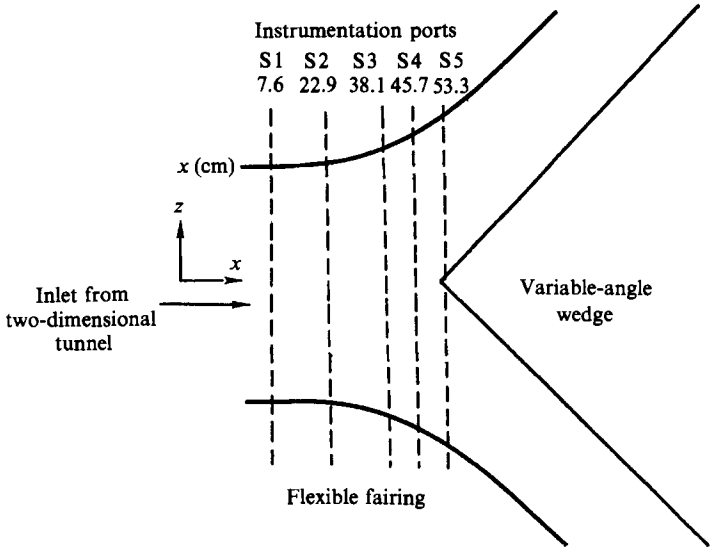

FIGURE 2. Sketch of test-section geometry.

pressure field set up by the wedge and fairings. The pressure field can be changed by varying the angle of the wedge and the position of the fairings.

The present paper focuses on the development of the Reynolds stresses as a perturbation from a two-dimensional boundary-layer state. Reynolds stress data from the two present experiments will be compared to each other and earlier data in an effort to determine the governing parameters for the Reynolds stress development. Some triple-product data will also be shown, mostly as a warning to Reynolds stress modellers. A full report (Anderson & Eaton 1987) provides a complete description of the experimental techniques as well as the extensive documentation of the mean flow field required for use of the data as a computational test case. All data presented here and in the full report are available on magnetic tape from the second author.

2. Equipment and techniques

The experiments were conducted in a three-dimensional test duct mounted on the end of a two-dimensional development section. The test duct consisted of two plane parallel walls separated by 11.9 cm and the wedge and fairings sketched in figure 2. The pressure field which drove the three-dimensionality was generated by the symmetrical wedge facing into the flow. Two different wedges were used; a 90° inclined angle wedge for Case I and a 60° inclined angle wedge for Case II. The pressure field was also affected by the position of two flexible fairings extending downstream from the development-section endwalls. The position of the fairings was selected to ensure a favourable pressure gradient and therefore thin boundary layers along the entire length of the fairing. The fairings were positioned using a template, resulting in a pressure field which was symmetrical about the centreline to within the measurement uncertainty. Repeated flow visualizations using a smoke wire upstream of the stagnation point showed that the free-stream flow was steady.

The inlet flow to the three-dimensional test section was supplied by a two-dimensional blower-driven wind tunnel with a 12.7 cm × 61 cm rectangular test section (Eibeck & Eaton 1985). The boundary layer of interest developed over a

length of 210 cm on one of the 61 cm walls of the test section. At the inlet to the three-dimensional test section the boundary layer was two-dimensional with the following integral parameters: $\delta_{99} = 3.12$ cm, $\theta = 0.36$ cm, $H = 1.35$, $C_f = 0.0032$ and momentum thickness Reynolds number = 3750 at 16.3 m/s free-stream velocity. The boundary layer on the wall opposite the test wall was removed using a scoop, reducing the test section depth to 11.9 cm. The free-stream turbulence level was approximately 0.2%.

The U- and W-mean velocity components were measured using a three-hole yaw probe which was fabricated from 0.8 mm OD round hypodermic tubing. The side tubes were cut at a chamfer angle of 40° relative to the probe tip axis following the recommendation of Bryer & Pankhurst (1971). The probe was calibrated to measure both the velocity magnitude and the flow angle without nulling the probe to determine the flow angle. The calibration was performed for a yaw angle range of $\pm 30°$. The probe was aligned approximately with the flow so that the measured flow angle was always within the range $\pm 25°$. A Young & Mass (1936)-type correction as implemented by Eibeck & Eaton (1985) was used to find an effective location of the probe tip based on the measured velocity gradient.

The six components of the Reynolds stress tensor, the ten triple products, and redundant measurements of the mean velocity components were measured using a conventional X-array hot-wire probe. The probe was a DISA 55-P-51 dual sensor tip having 3 mm long, 5 μm diameter wires. The wires were mounted with a spacing of 1 mm. Each wire was gold plated at the ends to achieve an active length of 1.25 mm. The probe was connected to two Precision Measurement Engineering Model 108 constant-temperature anemometers operating at a resistance ratio of 1.8. The bridge control circuit was balanced to give a system frequency response of 35 kHz. Each bridge output signal was low-pass filtered (Frequency Devices Model 901F) with a cutoff frequency of 20 Hz. The DC bias was removed and the signal amplified using a Precision Measurement Engineering Model 107 Buck and Gain. The filtered and amplified signal was then passed to the data acquisition system for digitization with 12-bit resolution.

The measured voltages from the hot-wire probe were interpreted assuming a 'cosine-law' response and neglecting the velocity component perpendicular to the plane of the wires. To minimize the uncertainty, the probe axis was aligned with the previously measured mean flow direction at each measurement point. Data were acquired in each of four different positions, the (U, V)-plane, the (U, W)-plane, and two 45° planes. The latter two positions were used only to measure quantities involving both v- and w-component fluctuations, namely $\overline{v'w'}$, $\overline{v'^2w'}$, $\overline{v'w'^2}$, and $\overline{u'v'w'}$.

The probe was calibrated in the free stream to determine the coefficients of a King's law response equation and the effective angle of the wires in each plane. The calibration was done under computer control and followed the technique outlined by Westphal & Mehta (1984). Calibrations were performed before and after each profile and the data discarded if the calibration changed by more than 1%. The flow temperature was measured before and after each measurement point and the Bearman (1971) temperature correction applied to each of the measured hot-wire voltages.

Uncertainties in cross-wire measurements arise from a variety of sources including the finite probe size, non-cosine response behaviour, out-of-plane velocity components, temperature drift, and calibration inaccuracies. The latter two uncertainty sources were minimized in the present experiment by frequent and automatic

recalibration. A complete analysis of the other uncertainty sources is difficult because of the anisotropic nature of boundary-layer turbulence. Estimates of the uncertainties due to the calibration and data reduction procedure and deviations from cosine-law response were reported in Anderson & Eaton (1987). The uncertainty in the mean velocity components was estimated as less than 2 % of the local value of U. This estimate was supported by comparisons to the three-hole-probe data at over 1000 measurement points. The worst deviation between the two measurement techniques was 1.8 %, with the typical deviation being about 1 %.

The uncertainty in the normal stresses was estimated to be 4 % of $\overline{u'^2}$. This estimate was supported by comparisons of data measured in the upstream boundary layer to the data of Klebanoff (1954) and Purtell, Klebanoff & Buckley (1982). Agreement of all three normal stresses was excellent outside $y/\delta = 0.1$. Inside this location, finite-probe-volume effects clearly become important. The active length of each wire was 2.6 % of the upstream boundary-layer thickness or approximately 50 viscous wall units. This length would be expected to cause some attenuation of the normal stresses near the wall (Johansson & Alfredsson 1983). The finite separation of the wires (2 % of the upstream boundary-layer thickness) causes a 'cross-talk' effect, increasing the measured value of $\overline{v'^2}$ near the wall (Nakayama & Westphal 1986). Our dimensionless wire length and spacing was similar to Nakayama and Westphal's Case 0, which apparently had relatively small cross-talk.

The estimate of uncertainty in the shear stress measurements was 8 % of the local value of $\overline{u'v'}$ outside $y/\delta = 0.1$. The uncertainty apparently increased rapidly approaching the wall. Measurements of $\overline{u'v'}$ in the two-dimensional boundary layer were compared to the data of Klebanoff (1954) showing excellent agreement. In a more recent test Pauley & Eaton (1988), using the same flow and hot-wire system, compared shear stress and triple product measurements with those reported by Murlis, Tsai & Bradshaw (1982) measured at the same Reynolds number. The shear stresses agreed within a few percent across the entire boundary layer. Agreement of the triple products was also excellent outside $y/\delta = 0.2$. The general reliability of the shear stress measurements is also illustrated by the fact that the $\overline{u'v'}$ shear stress extrapolates well to the wall shear stress value for all profiles shown below.

Measurements of the secondary shear stress $\overline{v'w'}$ are particularly sensitive to the out-of-plane velocity components. The probe was aligned with the mean velocity vector to within 1° at every measurement point to minimize this source of uncertainty. Alignment of the probe also minimized uncertainty due to flow interference by the prongs. This effect cannot be completely eliminated in a three-dimensional boundary layer, but was probably small since plated wires were used.

Measurement bias is caused by the difference in the height of the wires above the wall when the probe is positioned in the (U, W)-plane (wires parallel to the wall). For example, a normal gradient of the axial mean velocity component produces a signal which is interpreted as a positive spanwise velocity component. Similar biases are present in the measurement of $\overline{w'^2}$ and $\overline{u'w'}$. The bias is not an uncertainty in the strict sense and could potentially be corrected. However, the uncertainty in the bias correction is large so we chose to ignore it. Analysis of the mean velocity gradients indicates that the bias is small for measurement locations outside $Y = 3$ mm ($y/\delta = 0.1$).

Both of the probes described as well as a static pressure probe were positioned using a two-axis computer-controlled traverse which had an accuracy of 0.003 mm in y and 0.006 mm in z. The traverse also had the capability to rotate (yaw) the probes about the normal (y) axis. All probes were mounted on gooseneck stems so

that they could be yawed without translating the probe tip. The probes were inserted through slots at stations 1–5, labelled S 1–S 5 on figure 2. The slots were sealed with foam tape when a probe was in place and by a flush fitting plug at other times.

The skin friction vector was measured using a dual-fence probe described by Higuchi (1983). The height of the fence was 0.12 mm, which corresponded to 5 wall units in the upstream boundary layer. The gauge was calibrated in the two-dimensional inlet boundary layer over a range of free-stream velocites. A two-step measurement procedure was used in which the skin friction vector angle was first determined. The probe was then rotated so that one fence was normal to the skin friction for accurate determination of the vector magnitude. The uncertainty of this technique was estimated to be $\pm 3°$ for the skin friction angle and $\pm 5\%$ for the magnitude. Measurements were only possible for Case I because special port holes drilled in the test wall were required.

Experimental control and data acquisition was done by a DEC MINC microcomputer system which digitized all analog signals with 12-bit resolution. Pressure probe data were processed online. Raw hot-wire voltages were recorded on floppy disk and post-processed on a VAX 11/750 microcomputer.

3. Results and discussion

The results presented below are normalized by a reference velocity and pressure, respectively the free-stream velocity and static pressure on the tunnel centreline at the first measurement station ($x = 7.6$ cm, $z = 0$). The coordinate system used is usually the 'wind-tunnel coordinates' shown on figure 2. Coordinate values are not normalized because there is no consistent normalization for three-dimensional boundary layers and the normalization loses information about boundary-layer growth.

The free-stream static pressure distributions for the two cases with different wedge angle are shown in figures 3 and 4. The pressure coefficient is referenced to the pressure on the centreline at the first x-station and normalized by the dynamic pressure at that same location. In both cases there is a strong adverse pressure gradient on the centreline approaching the separation point upstream of the wedge. Off-centreline, the pressure gradient remains adverse through station S 4 then becomes favourable as the flow accelerates in the exit duct. A strong spanwise pressure gradient develops downstream of the first station and continues throughout the length of the test section. This spanwise pressure gradient causes the monotonic turning of the free stream and the secondary flow within the boundary layer. The main difference in the two pressure fields is that the streamwise pressure rise is somewhat greater in Case I. This leads to a greater retardation of the boundary-layer flow and a larger skewing angle between the free stream and the flow near the wall.

The overall development of the flow is best illustrated by mean velocity surveys which were measured using the three-hole probe. Spanwise surveys were made at five different y-locations for each of the seven x-stations. The free-stream plane and the plane nearest the wall ($y = 0.19$ cm, $y/\delta \approx 0.05$) are shown for the two cases in figures 5 and 6. In each figure, the longer vectors represent the free-stream flow and the shorter, more skewed vectors represent the plane nearer the wall. The free stream is turned rapidly by the pressure gradient and the boundary-layer skewing develops quickly. By the fourth station, the skew angle between the wall and the free stream is greater than 30°. The presence of a separation region in the vicinity of the wedge

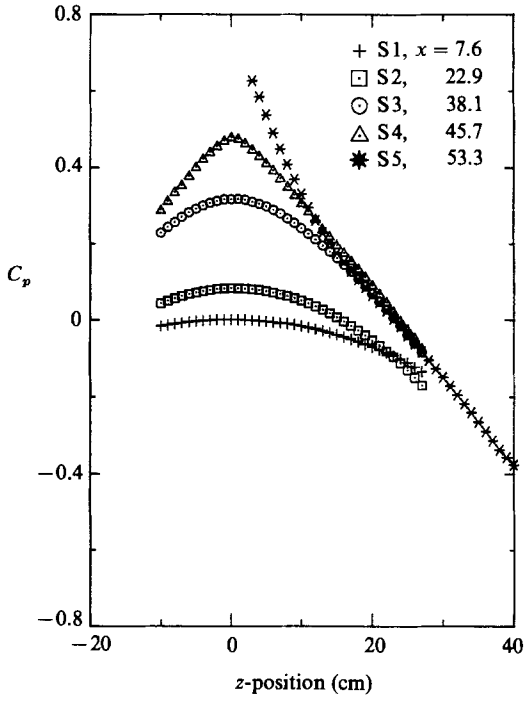

FIGURE 3. Static pressure coefficient for Case I.

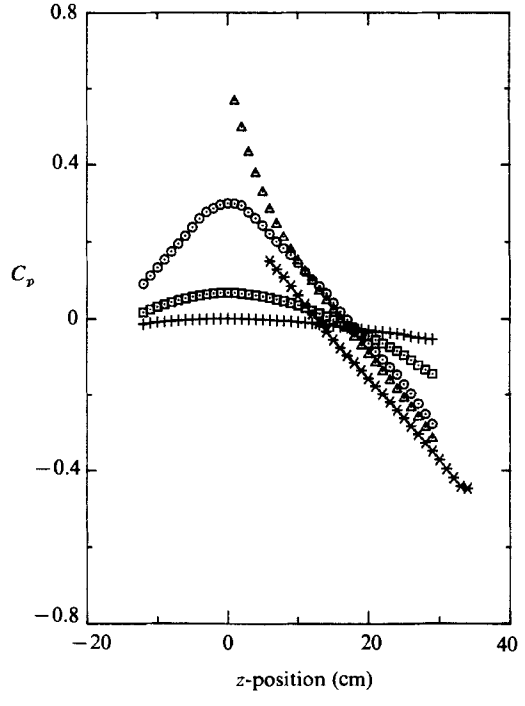

FIGURE 4. Static pressure coefficient for Case II. Symbols as in figure 3.

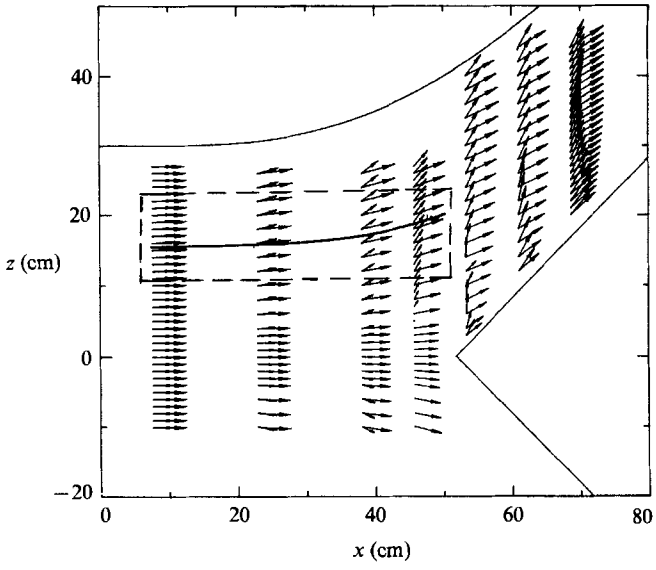

FIGURE 5. Mean velocity in (x, z)-planes for Case I. Longer vectors, $y = 6.0$ cm. Shorter vectors, $y = 0.19$ cm.

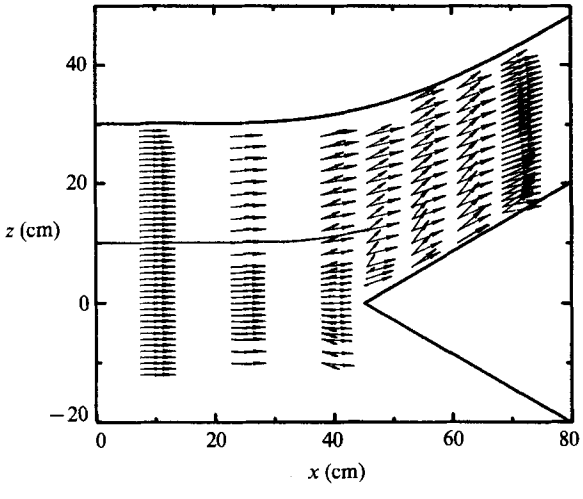

FIGURE 6. Mean velocity in (x, z)-planes for Case II. y-positions same as figure 5.

tip is obvious in the figures. It is also apparent from the figures and from three-component measurements not shown here that the flow at stations 6 and 7 is exceedingly complex. This downstream flow is a complex three-dimensional duct flow rather than a three-dimensional boundary layer. The downstream region will not be discussed further since the results are too complex to interpret in the present context.

The flow along one free-stream streamline was selected for detailed examination in order to restrict the measurements to manageable proportions. Table 1 shows the x- and z-coordinates of the profile locations for each case. Detailed profiles were then measured at the intersection of the streamline with each measurement port. The selected streamline for Case I originates at $z = 15$ cm at the first x-station as shown

Station	1	2	3	4	5
			Case I		
x	7.6	22.9	38.1	45.7	53.3
z	15.0	15.4	16.7	18.4	20.9
δ_{99} (cm)	3.15	3.55	3.84	4.08	4.16
			Case II		
x	7.6	22.9	38.1	45.7	53.3
z	10.0	10.1	10.6	11.7	13.6
δ_{99} (cm)	3.61	3.82	4.02	4.22	3.96

TABLE 1. Profile location on selected streamlines

on figure 5. This streamline was selected because it passes through the region of strong boundary-layer skewing but is in a region of relatively small spanwise gradients. Therefore, the boundary layer should be reasonably representative of boundary layers in 'infinite-swept'-type flows and the interpretation of the data should be straightforward. The spanwise gradients of all of the stress components are quite small through the fourth measurement station.

The approximation to infinite swept flow is not maintained through the fifth station. The reason for this is apparent in figure 7 which shows streamlines calculated from the mean velocity data at $y = 0.7$ cm ignoring any y-component of the velocity. The streamlines in this plane were selected for display since the peak in the turbulent kinetic energy profile occurs near $y = 0.7$ cm in the skewed boundary layer. The squares indicate the location of the profile measurements along the free-stream streamline. Figure 7 shows that flow arriving at the first four stations has developed in regions remote from the centreline. However, by station 5, the flow has come from regions very near the centreline where spanwise gradients may be large. Therefore, the turbulence at this station has developed in an entirely different type of straining field and is subject to the effects of spanwise divergence and longitudinal curvature. The large changes in the Reynolds stresses to be shown below are just an indication of the difference between different flow regions.

The streamline selected for Case II originates at $z = 10$ cm in the two-dimensional boundary layer. This streamline was selected closer to the centreline so the rate of turning of the free-stream velocity vector is approximately the same. The pressure gradient along the streamline is somewhat weaker in the second case as shown in figure 8. The spanwise pressure gradient is initially weaker in Case II but becomes slightly stronger at stations 4 and 5. The key difference between the two flows is in the amount of skewing between the free stream and the flow near the wall. Again, in Case II the profiles for stations 1–4 are approximately representative of infinite-swept-type flows while the flow at the fifth station is considerably more complex.

Mean velocity profiles for the two cases are shown in figures 9 and 10. The boundary-layer development is indicated by the growth of δ_{99} tabulated in table 1. The Case I profiles show a considerable retardation of the streamwise velocity component through the fourth measurement station with a corresponding rapid increase in the cross-stream velocity component. Profiles of the mean flow angle are plotted for Case I in figure 11 along with the measured wall angle. The skewing angle between the free stream and the wall increases rapidly to an angle of 45° by station 4. The pressure gradient becomes favourable between the last two stations, leading

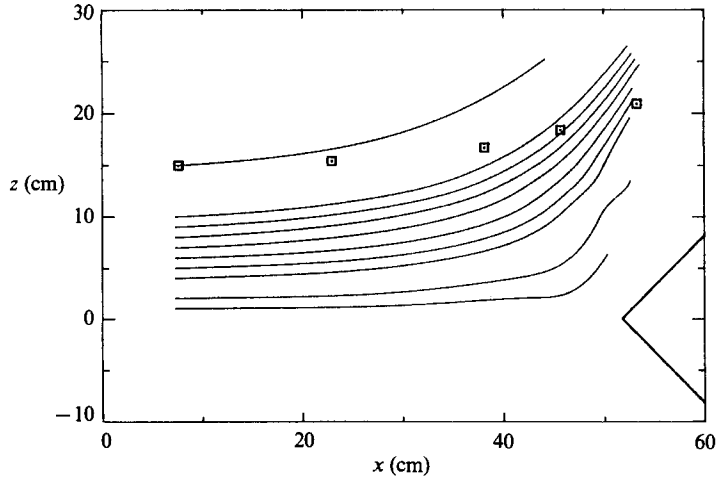

FIGURE 7. Calculated streamlines at $y = 0.7$ cm. Symbols indicate profile locations.

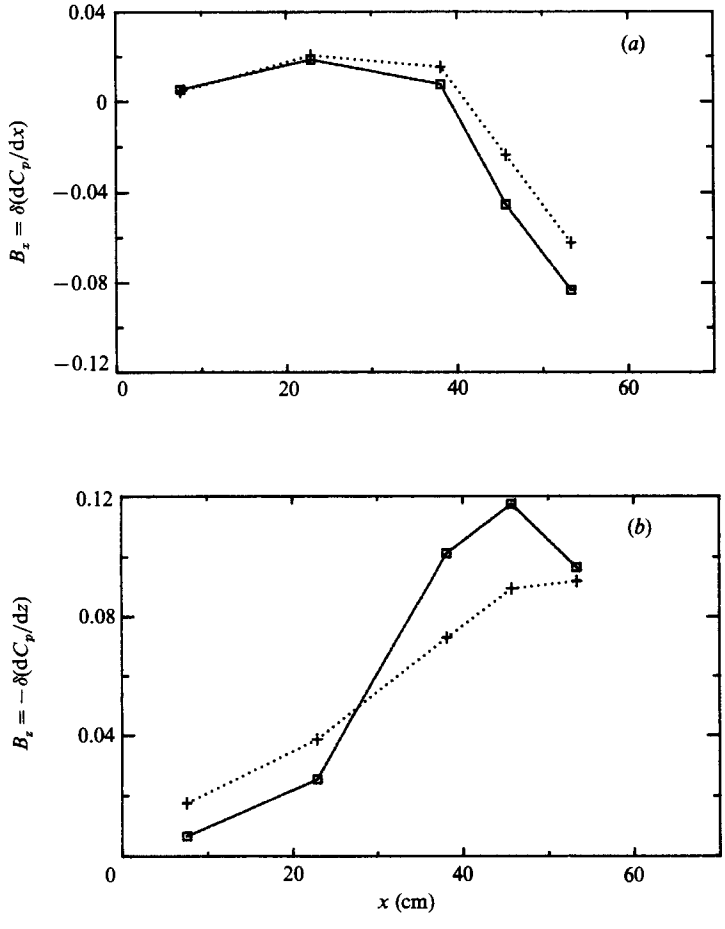

FIGURE 8. (*a*) Streamwise and (*b*) spanwise pressure gradient at the profile locations: +, Case I; □, Case II.

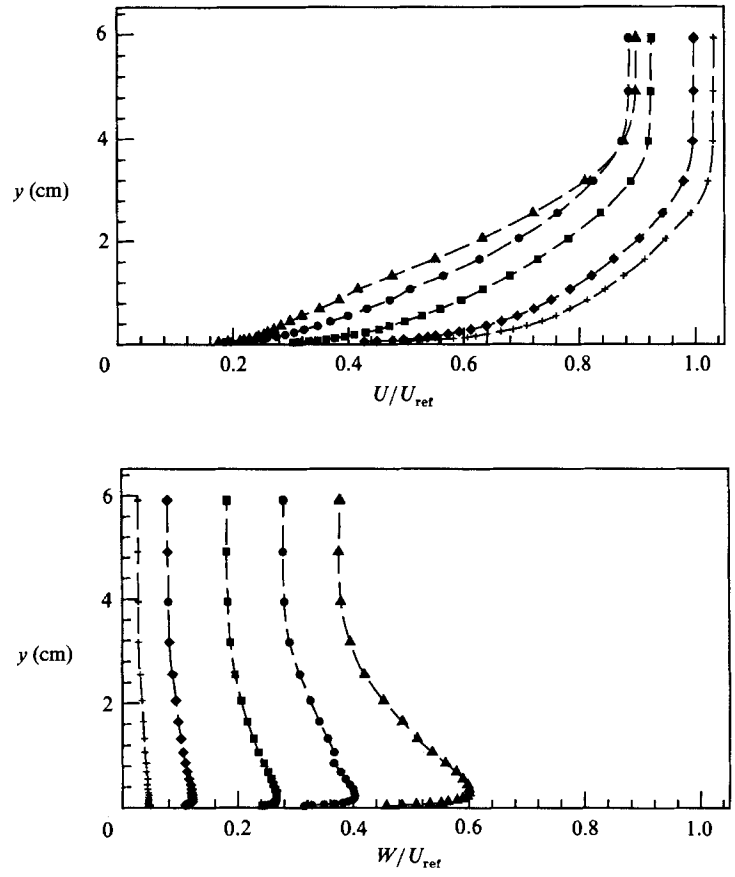

FIGURE 9. Mean velocity profiles for Case I: +, S1; ◆, S2; ■, S3; ●, S4; ▲, S5.

to the apparently anomalous behaviour in the inner region. The velocity profiles for Case II are only slightly retarded by the weaker pressure gradient. The skew angle is smaller but still quite significant. The wall angle is not available for Case II, but based on the velocity data we estimate a total skewing angle between the free stream and the wall of approximately 35° at station 4.

Profiles of all six components of the Reynolds stress tensor were measured at each station along the selected streamlines. The stresses are presented below in a coordinate system that is aligned with the wind-tunnel axis so that we can view the stress development as a perturbation of a two-dimensional boundary layer. The stresses are also normalized by a constant reference velocity, so the plots show absolute changes of the stress levels. Profiles at station 2 have been left out because they are only slightly different than the station 1 profiles and thus clutter the plots.

The turbulent kinetic energy profiles are shown in figure 12(*a*, *b*). The kinetic energy profile develops a peak away from the wall following the characteristic development in adverse-pressure-gradient boundary layers. The peak level grows slowly between stations 1 and 4 and then rapidly to station 5. The rapid change is an indication that we have entered a different region in the flow moving from station 4 to station 5. Detailed comparisons presented in Anderson & Eaton (1987) show that the data at station 5 compare well with the data of Dechow & Felsch (1977) and

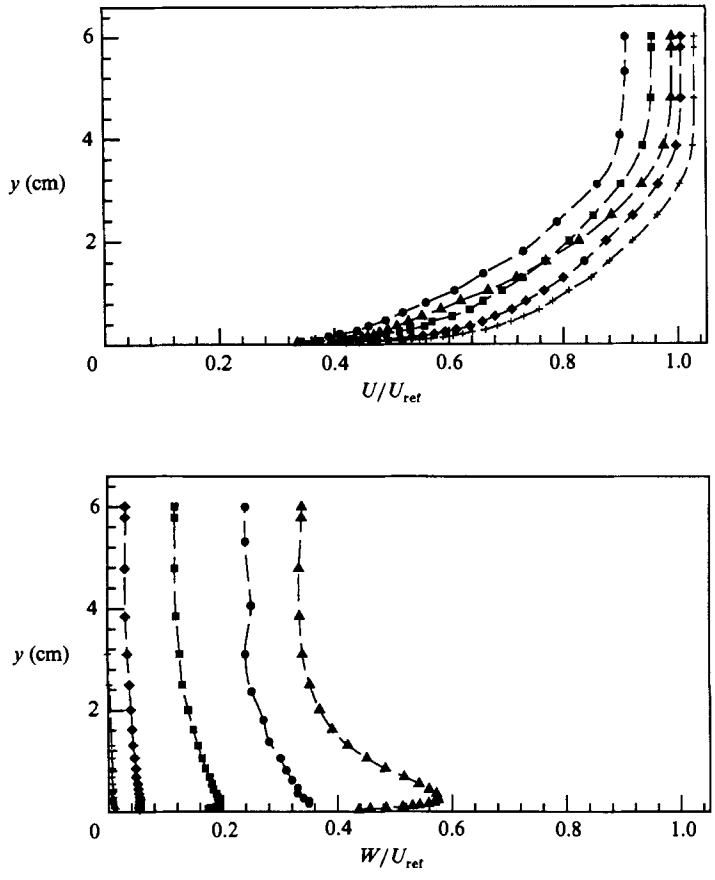

FIGURE 10. Mean velocity profiles for Case II. Symbols as in figure 9.

Muller (1982). Both of these flows are 'obstacle-type' flows where the initially two-dimensional boundary layer is deflected sideways by an obstacle. Such flows exhibit markedly different behaviour from the 'infinite-swept-wing' flows studied by Elsenaar & Boelsma (1974) and Bradshaw & Pontikos (1985).

The individual normal stress components are shown in figures 13–15. Both $\overline{u'^2}$ and $\overline{v'^2}$ develop a peak away from the wall which grows slowly to station 4 and then quite rapidly to station 5. The $\overline{w^2}$ profiles develop a different shape with a flat region adjacent to the wall which extends into the wake region. The levels of $\overline{w'^2}$ double between the 4th and 5th stations, emphasizing the strong differences between the flow regions.

The three shear stress components are shown in figures 16–18. The $\overline{u'v'}$ shear stress shows a development very similar to a two-dimensional adverse-pressure-gradient boundary layer in that the $\overline{u'v'}$ level near the wall falls rapidly in response to the decrease in the skin friction level. The skin friction was measured at each profile location for Case I and the streamwise component is indicated on the vertical axis of figure 16. It is apparent that the measured $\overline{u'v'}$ values asymptote to the local skin friction level. The inner layer of reduced shear stress grows outward, leaving a peak in the wake region of the boundary layer. The peak level in each profile remains approximately the same. The reduction in the shear stress is not as strong as in Case II which has a lower skewing angle and thus a higher streamwise component of the

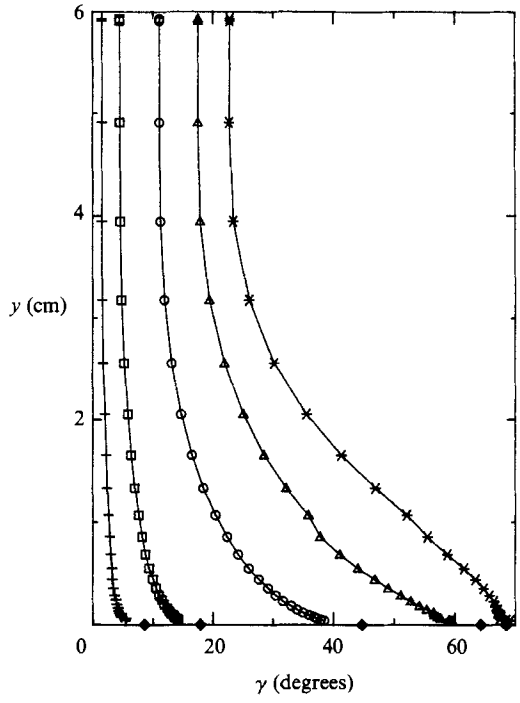

FIGURE 11. Mean flow angle relative to fixed 'wind-tunnel' coordinate system. Solid symbols on abscissa indicate measurements with surface-fence probe: +, S1; □, S2; ○, S3; △, S4; ✳, S5.

skin friction. The peak value in each profile also occurs closer to the wall in Case II.

The spanwise shear stress component, $\overline{v'w'}$ shown in figure 17 is plotted on the same scale as $\overline{u'v'}$ to facilitate comparison between the shear stress components. The spanwise component has much lower levels than the streamwise shear stress at all stations even though normal velocity gradients of U and W are comparable. The cross-stream shear stress profiles exhibit thick 'constant stress layers' at stations 3 and 4 for both cases. The outer edge of the constant stress layer corresponds roughly to the location of the peak of the $\overline{u'v'}$ profile. At station 5, the profile is highly distorted with very low overall shear stress levels. The spanwise component of the skin friction is plotted on the left boundary of figure 17. The level of the shear stress in the constant stress layer is far below the skin friction, indicating that any analogy to the constant stress layer in a two-dimensional boundary layer is inappropriate. Very large gradients in the spanwise shear stress must exist below the lowest measurement point. It is not known if the $\overline{v'w'}$ levels increase rapidly adjacent to the wall or if there is an unusually large viscous component of the shear stress. It will be shown below that the normal transport of the $\overline{v'w'}$ shear stress by turbulence is extremely rapid. This rapid transport is apparently responsible for the constant stress layer. It seems unlikely that a thin region of high $\overline{v'w'}$ could exist under these conditions.

The spanwise shear stress profiles for Case II are very similar to Case I although the maximum levels are slightly lower. The constant stress layer is also thinner in Case II. Again in Case II, the outer edge of the constant stress layer is at approximately the same location as the peak in $\overline{u'v'}$.

The third component of shear stress, $\overline{u'w'}$ is shown in figure 18 for completeness.

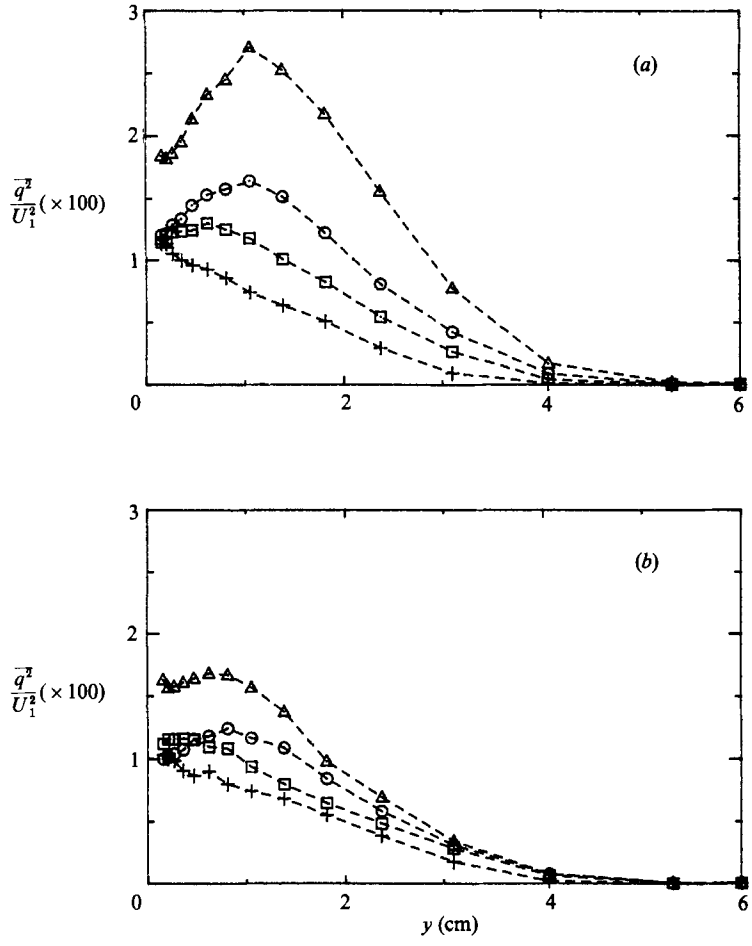

FIGURE 12. Turbulence kinetic energy profiles: +, S1; □, S3; ○, S4; △, S5; (*a*) Case I; (*b*) Case II.

The important shear stress components in attached boundary-layer flows are those in the plane of the wall, namely $\overline{u'v'}$ and $\overline{v'w'}$. Pierce & Ezekewe (1976) found that x- and z-gradients of $\overline{u'w'}$ were significantly smaller than y-gradients of $\overline{u'v'}$ and $\overline{v'w'}$ even in a flow with very high levels of $\overline{u'w'}$. Figure 18 shows that the $\overline{u'w'}$ stress remains small through the 4th station. The levels are considerably larger in the highly distorted flow at station 5.

The ratio of the shear stress magnitude to twice the turbulent kinetic energy (commonly called A_1) is a useful quantity in two-dimensional boundary layers. A_1-values are typically close to 0.15 even in distorted boundary layers. A_1 is useful in three-dimensional boundary layers if it is defined as

$$A_1 = [(\overline{u'v'})^2 + (\overline{v'w'})^2]/q^2,$$

where

$$q^2 = \overline{u'^2} + \overline{v'^2} + \overline{w'^2}.$$

A_1 thus defined is invariant to coordinate rotations around the vertical (y) axis. Bradshaw & Pontikos (1985) observed a strong decrease in A_1 in their infinite-swept-wing experiment. The same effect is found in the present experiments as indicated

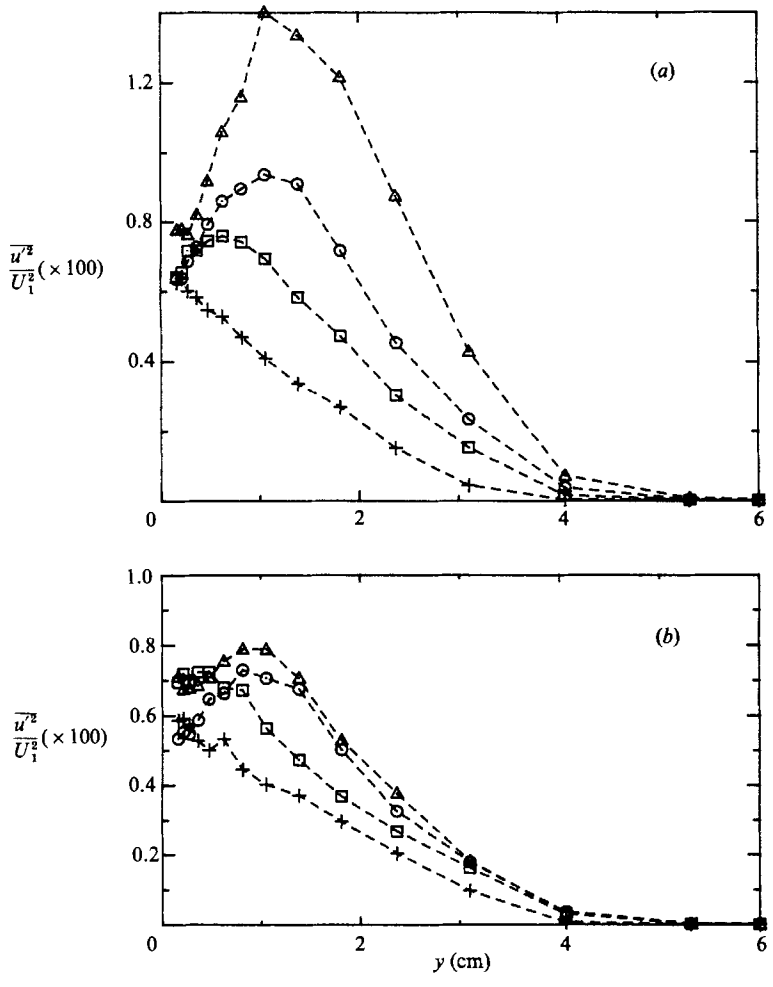

FIGURE 13. Profiles of $\overline{u'^2}$. Symbols as in figure 12. (*a*) Case I; (*b*) Case II.

in figure 19(*a*, *b*). A_1 decreases monotonically in both cases except near the outer edge of the boundary layer where it remains approximately constant. The decrease in A_1 is more rapid in the more strongly skewed Case I. The implication is that a more strongly skewed boundary layer will exhibit lower levels of the shear stress/kinetic energy ratio. The experiments of Bradshaw & Pontikos (1985) and Baskaran & Bradshaw (1987*b*) follow the same trend. Their boundary layers are more weakly skewed than Case II and the decrease in A_1 are proportionately smaller with the lone exception of the final measurement station of Bradshaw & Pontikos which exhibits a very strong decrease in A_1.

Johnston (1976) and van den Berg (1982) examined the ratio of the spanwise to the streamwise eddy viscosity in their review articles. The ratio is commonly called N_e and is defined as

$$N_e \triangleq \frac{\tan(\gamma_\tau - \gamma_{fs})}{\tan(\gamma_g - \gamma_{fs})},$$

where γ_τ is the angle of the shear stress vector in a coordinate system aligned with the free stream, γ_g is the angle of the velocity gradient vector in the free-stream

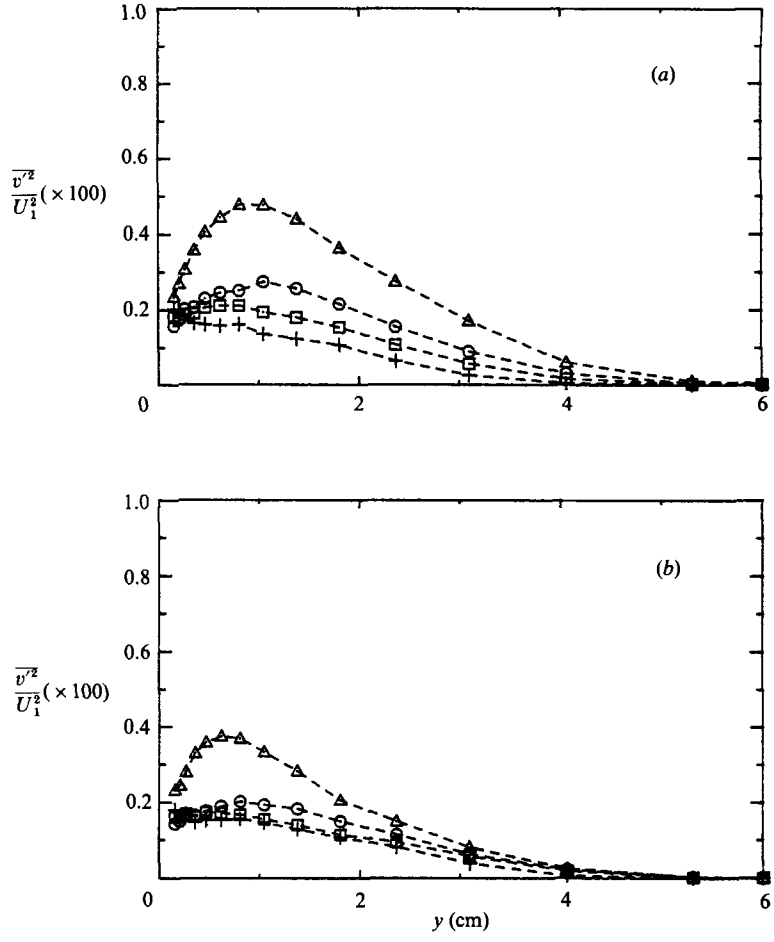

FIGURE 14. Profiles of $\overline{v'^2}$. Symbols as in figure 12. (*a*) Case I; (*b*) Case II.

coordinate system, and γ_{fs} is the angle of the mean velocity vector in the free-stream coordinate system.

The eddy viscosity ratio is plotted in figure 20 for stations 4 and 5 of both cases. The ratio is very small at stations further upstream. Also shown on figure 20 are data from Elsenaar & Boelsma (1974), Pontikos (1982), and Dechow & Felsch (1977). Scatter in the data is large because the calculation of the eddy viscosities requires differentiation of experimental data. However, the trends are clear; rapidly turned experiments such as the present flows exhibit low values of the eddy viscosity ratio. The more slowly turned flows such as the two infinite-swept-wing flows illustrated on figure 20 exhibit much higher values of the ratio.

Unfortunately, there are not enough data to postulate a quantitative relationship between the eddy viscosity ratio and the free-stream turning rate. To gain some insight a non-dimensional turning rate defined as the boundary-layer thickness divided by the radius of curvature of the free-stream streamline was estimated for each of the five experiments shown. The present two flows have non-dimensional turning rates of approximately 0.05. The turning rate varies strongly in the Dechow & Felsch experiment but the value is approximately 0.03 in the region of interest. The turning rate in the infinite-swept-wing experiments is approximately 0.01. The

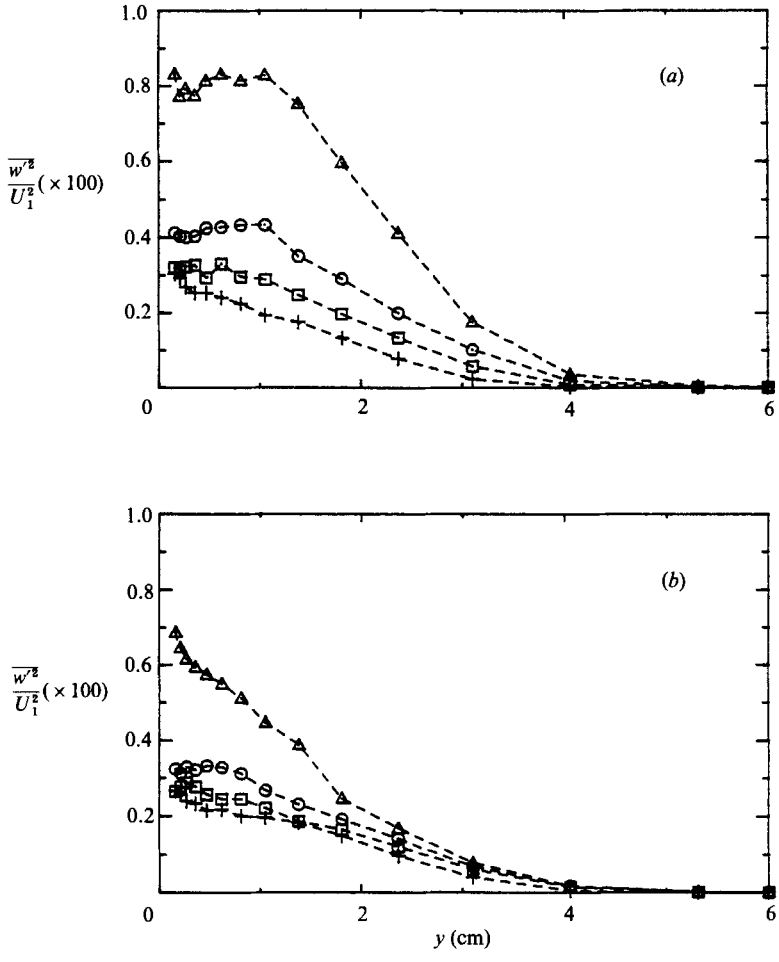

FIGURE 15. Profiles of $\overline{w'^2}$. Symbols as in figure 12. (*a*) Case I; (*b*) Case II.

present sparse data indicate that the eddy viscosity ratio varies from values near 1 at a turning rate of about 0.1 to a value around 0.2 for turning rates above 0.03. More experiments are needed to determine the values of the ratio at intermediate turning rates.

The previous paragraphs lead one to the conclusion that a full stress equation model is needed to accurately calculate three-dimensional boundary-layer flows. Such a model requires that all terms of the Reynolds stress transport equations must be either calculated or modelled. One particular set of terms that must be modelled are the triple velocity correlations which may be interpreted as the turbulent transport of the Reynolds stresses. All ten triple products were calculated from the raw data for Case I to gain some insight into the required modelling. It should be emphasized that all terms of the Reynolds stress transport equations cannot be calculated from the present data. Only a selection of the plots and some derived quantities are shown here. The full set of triple products is available on request from the authors.

Triple products are shown for the first four stations along the test streamline. Between stations 1 and 4, the triple products develop smoothly as a perturbation

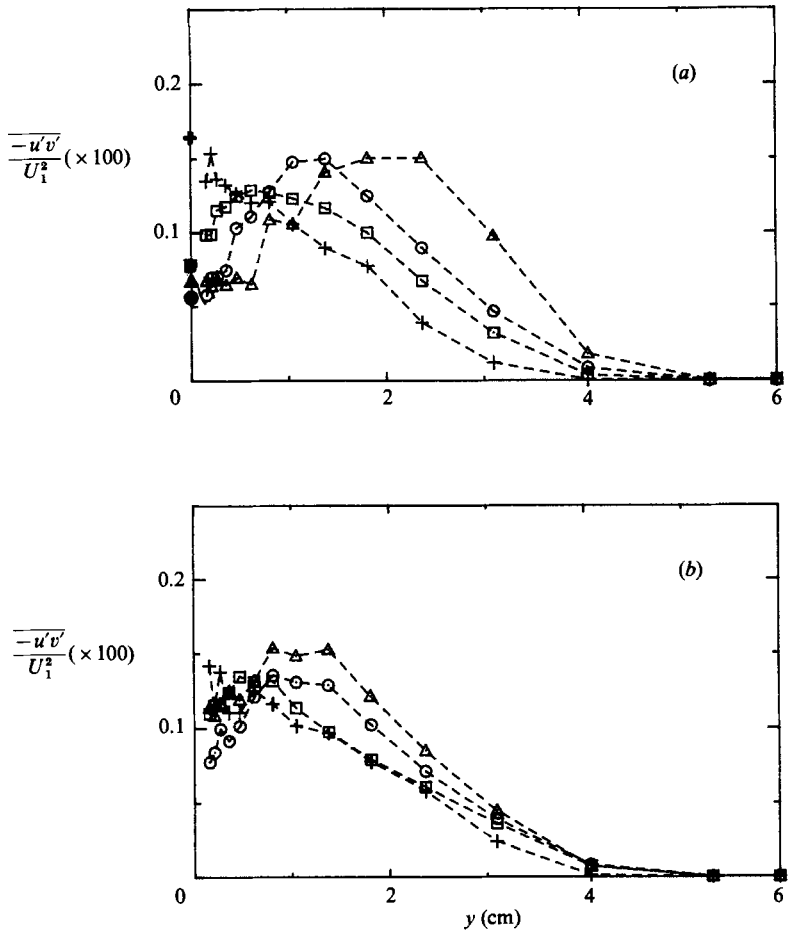

FIGURE 16. Profiles of $\overline{u'v'}$. Symbols as in figure 12. Solid symbols on ordinate indicate x-component of the wall shear stress. (*a*) Case I; (*b*) Case II.

from the two-dimensional boundary-layer state. Between stations 4 and 5, the triple products change rapidly as do the Reynolds-stress profiles. It is difficult to make any sensible interpretation of the data at station 5; therefore they have been eliminated to simplify the figures. The profiles of the four triple products involving only u- and v-velocity fluctuations were compared at the first station with the data of Murlis *et al.* (1982) measured in a two-dimensional zero-pressure-gradient flow. The agreement with both the profile shapes and the maximum values was good for all four quantiies.

Following Bradshaw & Pontikos (1985), the first quantity shown (figure 21) is the y-component transport velocity for the turbulent kinetic energy, which is defined as

$$Vq^2 = (\overline{u'^2v'} + \overline{v'^3} + \overline{v'w'^2})/q^2.$$

The transport velocity in the wake region remains nearly unchanged from S 1 to S 4, the scatter at the outer two points at the first station being caused by large uncertainty near the edge of the boundary layer. This result is in contrast to Bradshaw & Pontikos (1985) who observed a substantial decrease in the outer-layer

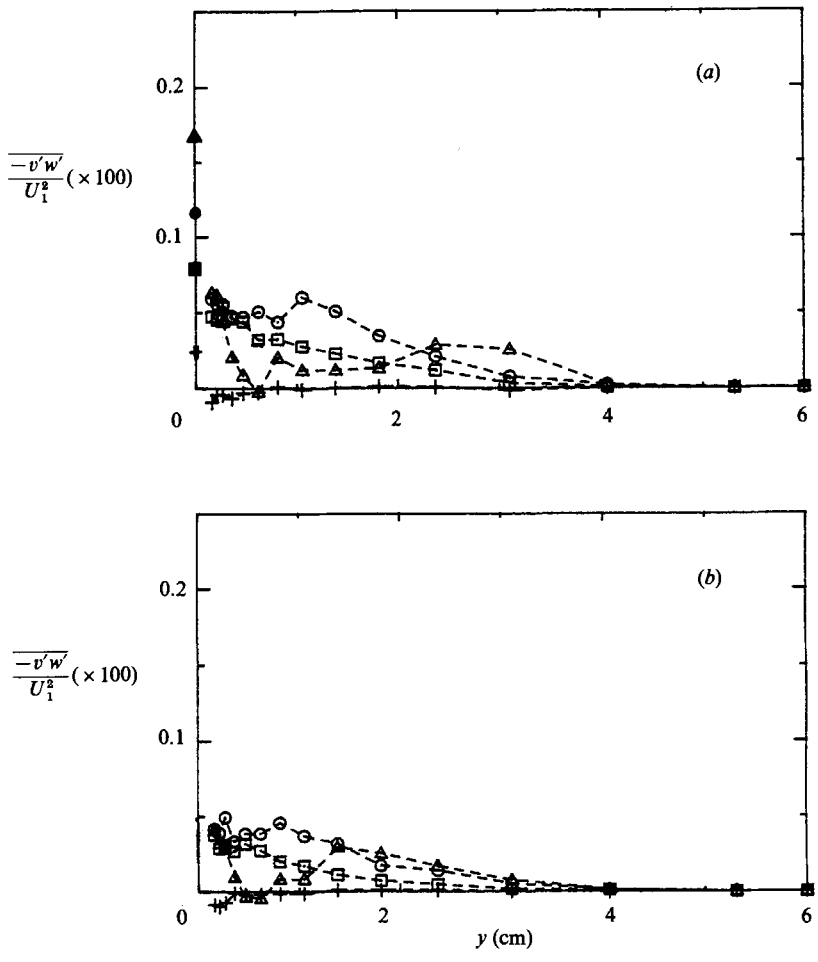

FIGURE 17. Profiles of $\overline{v'w'}$. Symbols as in figure 12. Solid symbols on ordinate indicate z-component of the wall shear stress.

transport velocity. Closer to the wall, the transport velocity falls rapidly after the second station, becoming negative by station 4. This negative loop is similar to the behaviour observed in two-dimensional adverse-pressure-gradient boundary layers and is related to the positive gradient of q^2 close to the wall. The overall profile development and the actual values of the transport velocity are in quite good agreement with the recent work of Baskaran & Bradshaw (1987*b*) in three-dimensional boundary layers with both concave and convex longitudinal curvature. One difference was that they observed some growth of the transport velocity in the outer layer.

Figure 22(*a–c*) presents the individual triple products forming the kinetic energy transport velocity. We see that the negative velocity at S 4 is due to a large negative value of the transport velocity of $\overline{u'^2}$. The transport velocity of $\overline{v'^2}$ is nearly zero near the wall at the fourth station and the transport velocity of $\overline{w'^2}$ is everywhere small. As an aside, it has often been assumed that $\overline{v'w'^2}$ is equal to $\frac{1}{2}(\overline{v'u'^2}+\overline{v'^3})$ in a two-dimensional boundary layer. However, $\overline{v'w'^2}$ is much smaller than $\overline{v'^3}$ in a two-dimensional boundary layer, a fact that can be understood by simple kinematic

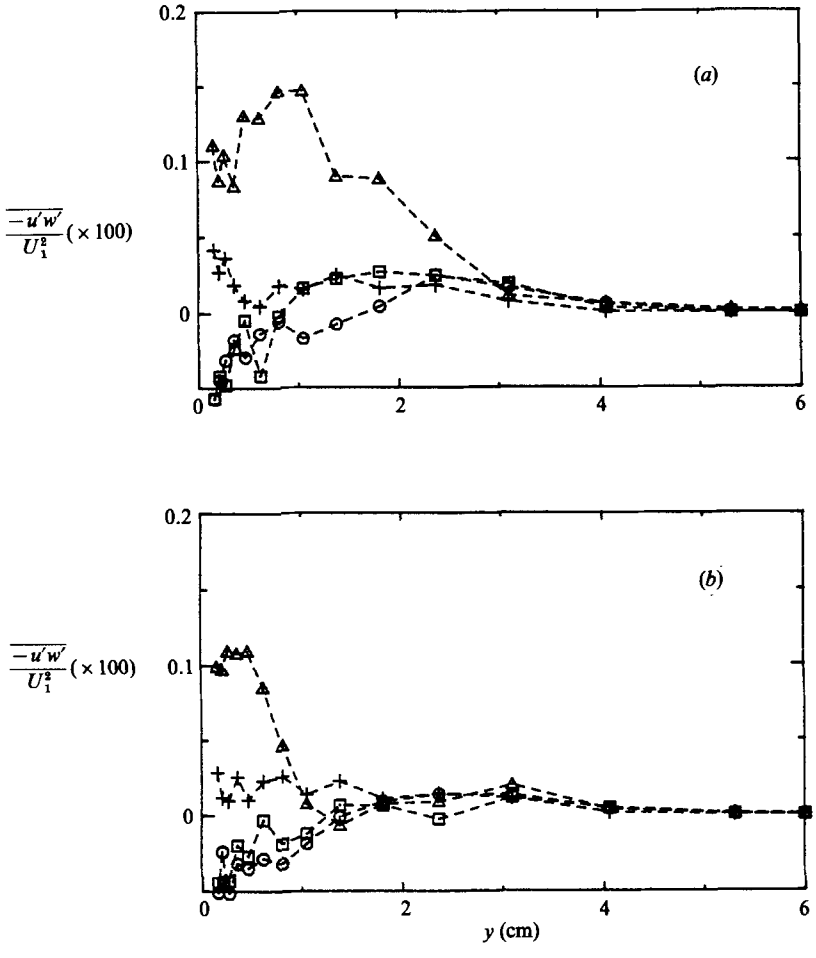

FIGURE 18. Profiles of $\overline{u'w'}$. Symbols as in figure 12.

arguments. We envision two types of motion which will produce large instantaneous values of $\overline{v'w'^2}$ as sketched in figure 23. The first 'burst-like' motion will produce a positive contribution to $\overline{v'w'^2}$ when averaged across the span. The second 'sweep-like' motion produces a negative contribution. Such motions are likely to occur with roughly equal probability, meaning that the average value of $\overline{v'w'^2}$ will be small.

In the present case, $\overline{v'w'^2}$ remains small throughout the flow development, making only a small contribution to the vertical transport of turbulent kinetic energy. This is somewhat surprising in view of the development of $\overline{v'^2w'}$ to be discussed below. However, a similar slow development was observed by Baskaran & Bradshaw (1987*b*).

The vertical transport of the two important shear-stress components, $\overline{u'v'}$ and $\overline{v'w'}$, are presented as raw triple products in figure 24(*a*, *b*). Figure 24(*a*) shows $\overline{u'v'^2}$ or the normal transport of the $\overline{u'v'}$ shear stress. The profiles at the first two stations show the typical behaviour found in two-dimensional boundary layers. By station 3 there is a significant region of positive $\overline{u'v'^2}$ (downward transport of $-\overline{u'v'}$). This positive region near the wall becomes quite large by station 4. Again, this observation is in qualitative agreement with the gradient transport hypothesis.

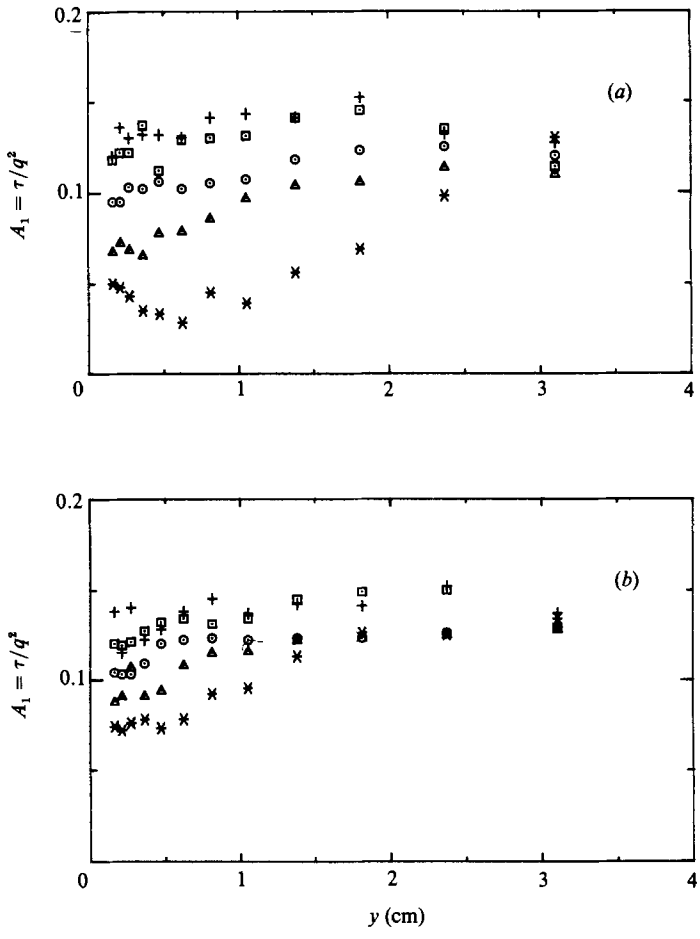

FIGURE 19. Profiles of the A_1 parameter: +, S1; ⊡, S2; ⊙, S3; △, S4; ✱, S5. (*a*) Case I; (*b*) Case II.

The rapid reduction in the shear stress near the wall leads to a substantial positive gradient of $-\overline{u'v'}$. The triple-product profile is changed very little in the wake region.

The vertical turbulent transport of the $\overline{v'w'}$ shear stress, namely $\overline{v'^2w'}$, starts out at the expected value of zero in the two-dimensional boundary layer. The transport grows rapidly until at the fourth station the profiles of $\overline{u'v'^2}$ and $\overline{v'^2w'}$ are almost the same. This result is somewhat surprising because the secondary shear stress, $\overline{v'w'}$ grows so slowly and the gradients of $\overline{v'w'}$ are always small relative to gradients of the primary shear stress. Gradient transport models for the Reynolds stresses would obviously fail in this flow. It is interesting to note that while the spanwise eddy viscosity component is much smaller than the streamwise component, the gradient transport constant is much larger for the spanwise shear stress than for the streamwise.

Not shown are the triple products that relate to spanwise transport of the various stress components. Generally these terms are of the order of $\frac{1}{3}$ of the corresponding vertical transport terms, indicating that the flow along the streamline approximates an infinite swept flow. The anomaly is in the transport of $\overline{u'^2}$. At the fourth station, there are several points in the inner half of the boundary layer where $\overline{u'^2w'}$ is nearly

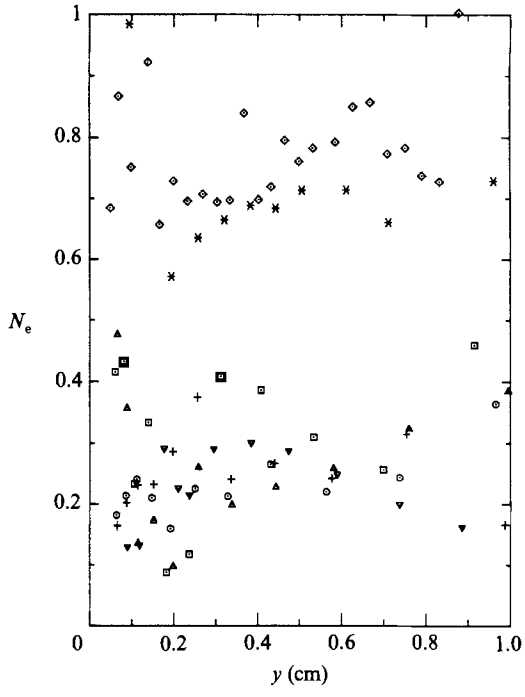

FIGURE 20. Eddy viscosity ratio for a coordinate system aligned with the local mean velocity. +, Case I, S4; ⊡, Case I, S5; ⊙, Case II, S4; △, Case II, S5; ✳, Pontikos (1982), S9; ◇, Elsenaar & Boelsma (1974), S9; ▽, Dechow & Felsch (1977), S4.

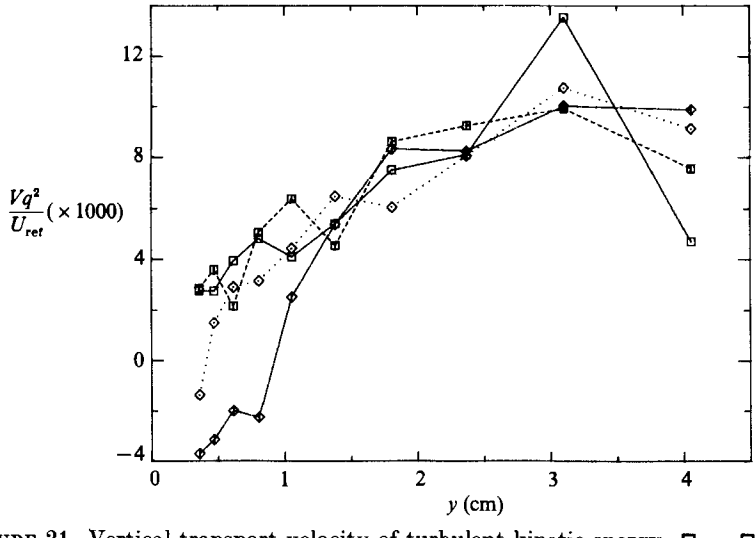

FIGURE 21. Vertical transport velocity of turbulent kinetic energy. □——□, S1; ⊡·····⊡, S2; ◇····◇, S3; ◇—◇, S4.

as large as $\overline{u'^2v'}$. The $\overline{u'^2w'}$ triple product is almost exactly zero in the outer half of the boundary layer and is small at the other three stations. The large values of $\overline{u'^2w'}$ do not necessarily imply that there is net spanwise transport of $\overline{u'^2}$. Similar levels of $\overline{u'^2w'}$ have also been observed in infinite swept flows.

Finally of interest are the u- and w-component skewnesses, $\overline{u'^3}$ and $\overline{w'^3}$, shown in

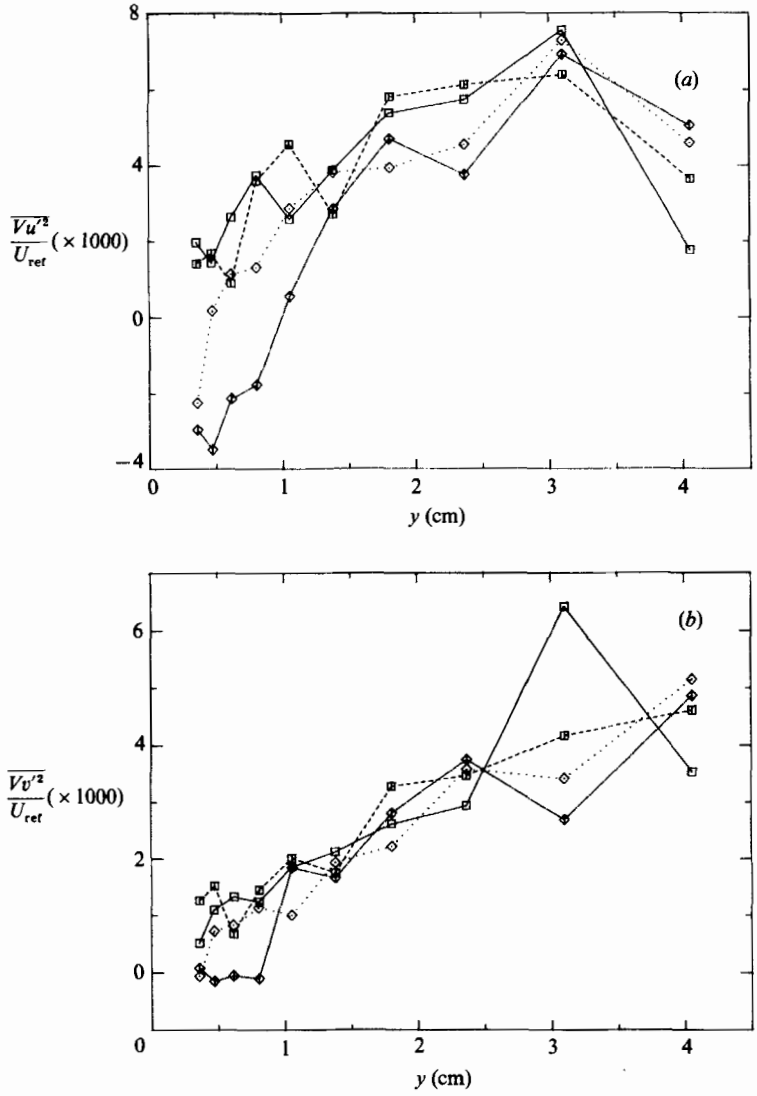

FIGURE 22(a, b). For caption see facing page.

figures 25 and 26 respectively. The u-skewness starts off with a normal two-dimensional boundary-layer profile. Both the positive and negative extrema grow rapidly, increasing by at least a factor of 3 between stations 1 and 4. The w-skewness starts out quite close to zero as would be expected. It grows slowly and by the fourth station its maximum value is only a small fraction of $\overline{u'^3}$. This latest result is a clear indication that the turbulence structure is not in equilibrium with the mean velocity field.

4. Comparison to Rotta T model

Rotta (1979) introduced a family of turbulence models for application in complicated three-dimensional flows. The focus of the model is the behaviour of the pressure–strain terms of the Reynolds-stress transport equations. Inherent in his

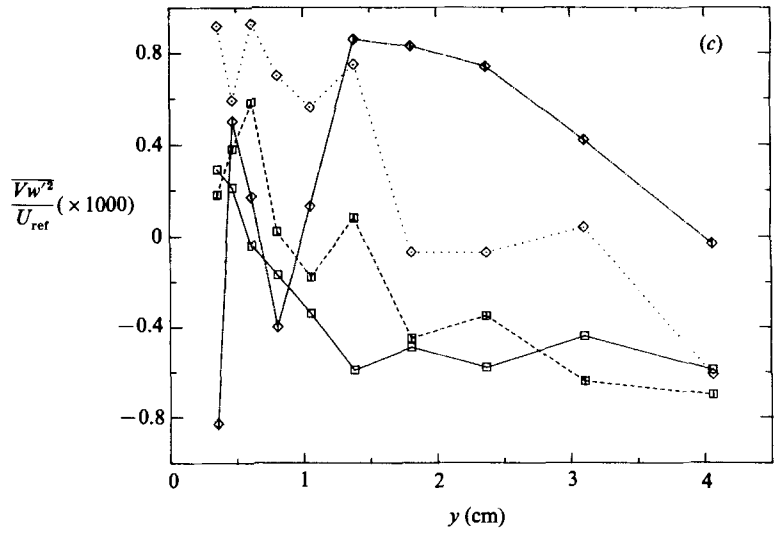

FIGURE 22. Vertical transport velocity of (*a*) $\overline{u'^2}$, (*b*) $\overline{v'^2}$, (*c*) $\overline{w'^2}$. Symbols as in figure 21.

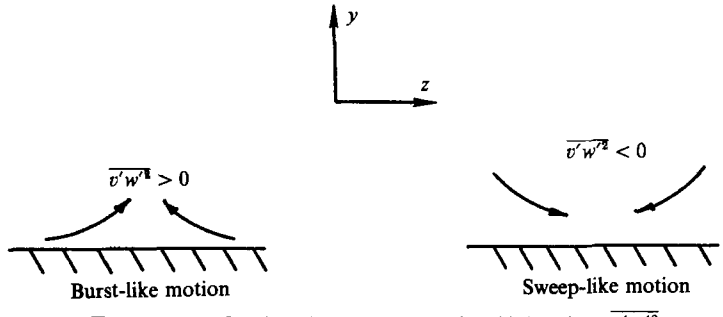

FIGURE 23. Qualitative argument justifying low $\overline{v'w'^2}$.

modelling of the pressure–strain terms is the assumption that the turbulence is isotropic with respect to a reference frame linked to the mean velocity vector. The resulting model is not invariant to coordinate translation; however, its application to the present flow is straightforward.

Rotta (1979) and later Abid & Schmitt (1985) incorporated the so-called Rotta T model into a mixing length model which will be compared to the present data. The essential feature of the model is an estimation of an eddy viscosity magnitude as given by

$$\nu_T = F^2 l^2 \left[\left(\frac{\partial U}{\partial Y}\right)^2 + \left(\frac{\partial W}{\partial Y}\right)^2 + \frac{T-1}{U^2+W^2}\left(W\frac{\partial U}{\partial Y} + U\frac{\partial W}{\partial Y}\right)^2\right]^{\frac{1}{2}}, \tag{1a}$$

where

$$l = 0.085\delta \tanh\left(\frac{0.41}{0.085}\frac{Y}{\delta}\right), \tag{1b}$$

$$F = 1 - \frac{1}{e^{y^+/A^+}}. \tag{1c}$$

The mixing length is based on a standard form, reducing to $l = ky$ near the wall, and the damping factor F is the Van Driest damping function. The Rotta model

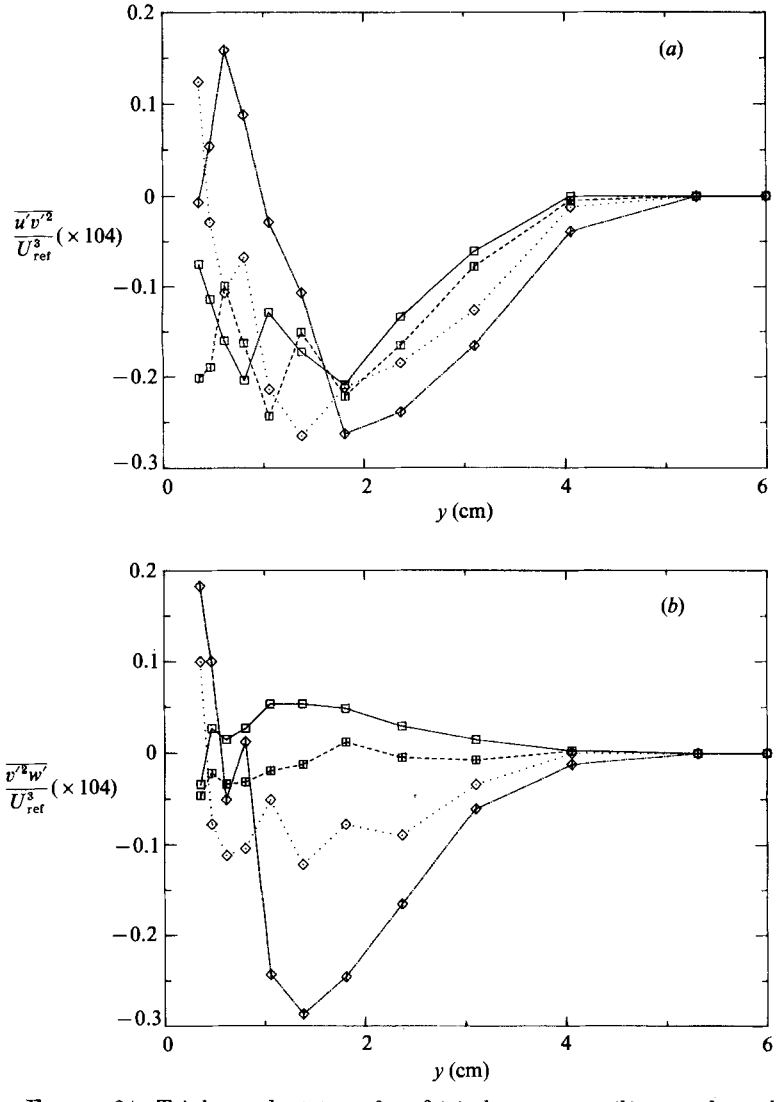

FIGURE 24. Triple product transfer of (*a*) shear stress, (*b*) secondary shear stress.

distributes the eddy viscosity magnitude as a vector quantity to calculate the streamwise and cross-stream shear stresses:

$$-\overline{u'v'} = \nu_{T,xx}\frac{\partial U}{\partial Y} + \nu_{T,xz}\frac{\partial W}{\partial Y}, \tag{2a}$$

$$-\overline{v'w'} = \nu_{T,zx}\frac{\partial U}{\partial Y} + \nu_{T,zz}\frac{\partial W}{\partial Y}, \tag{2b}$$

where

$$\nu_{T,xx} = \nu_T\left(\frac{U^2 + TW^2}{U_\tau^2}\right), \tag{2c}$$

$$\nu_{T,xz} = \nu_{T,zx} = \nu_T(1-T)\frac{UW}{U_\tau^2}, \tag{2d}$$

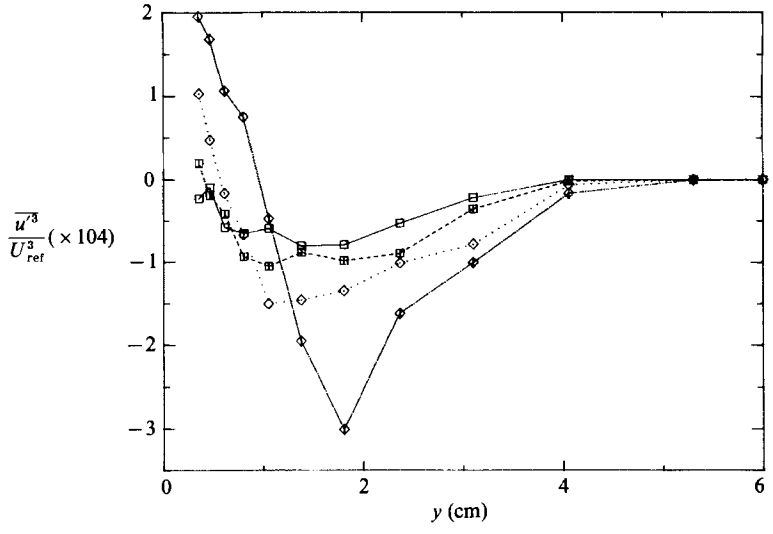

FIGURE 25. u-Component skewness. Symbols as in figure 21.

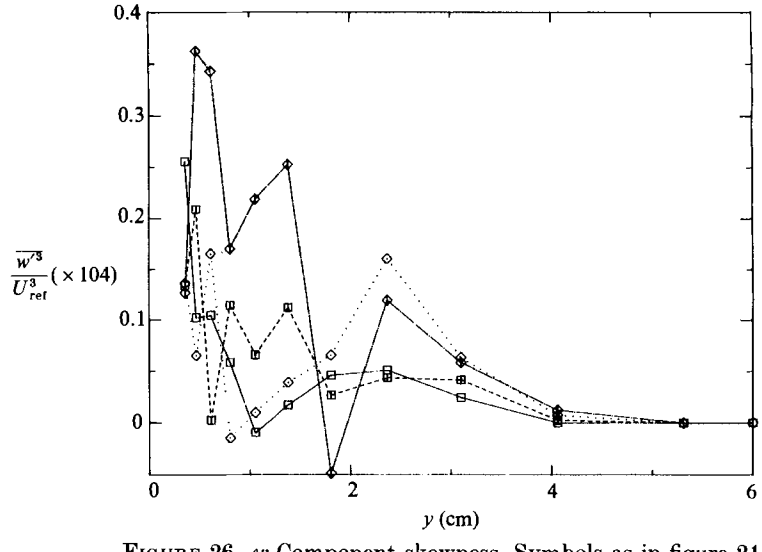

FIGURE 26. w-Component skewness. Symbols as in figure 21.

$$\nu_{T,zz} = \nu_T\left(\frac{W^2 + TU^2}{U_r^2}\right), \tag{2e}$$

$$U_r^2 = U^2 + W^2. \tag{2f}$$

The parameter T is analogous to the eddy viscosity ratio N_e discussed above. When T is 1.0, the model reduces to an istropic eddy viscosity.

The model was applied to the measured mean velocity profiles for both cases. Sensitivity tests showed that the model was insensitive to the value of A^+ so a constant value of $A^+ = 25.0$ was chosen for all computations. The value of T was varied from 0.2 to 1.0 in different computations. As expected, the value $T = 1.0$ gave the best fit to the data at the initial station where the boundary layer is two-

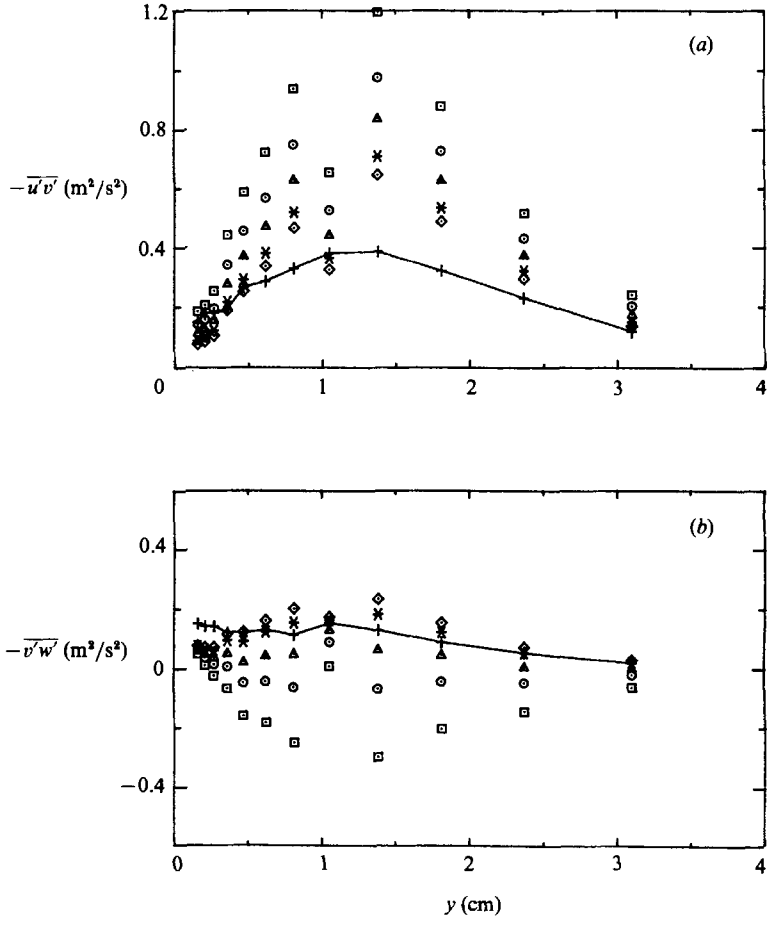

FIGURE 27. Comparison of Rotta T model predictions with data from Case I, Station S 4. Solid line indicates data; symbols, predictions for various values of T: ⊡, Rotta $T = 1.0$; ⊙, 0.7; △, 0.5; ✱, 0.3; ◇, 0.2. (*a*) $\overline{u'v'}$ stress; (*b*) $\overline{v'w'}$ stress.

dimensional. Figure 27 shows the measured and calculated shear-stress profiles at station 4 for Case I. The isotropic eddy viscosity calculations ($T = 1.0$) predicted values of $\overline{u'v'}$, which were too large by a factor of about 3. The secondary shear stress magnitude was much too large and the sign was wrong. There was a steady improvement in both profiles as T was decreased until relatively good agreement was achieved using $T = 0.2$. Similar results were found for Case II. Thus, a value of T equal to the eddy viscosity ratio N_e defined above seems to give a reasonable prediction of the shear stress profiles. T is exactly equal to the eddy viscosity ratio in a coordinate system aligned with the local mean velocity but such a coordinate system was not used here.

5. General discussion and conclusions

The measurements presented here are in general agreement with previous measurements in infinite-swept-wing-type flows. The shear stress vector composed of the $\overline{u'v'}$ and $\overline{v'w'}$ components of the Reynolds stress tensor is seen to lag behind the strain rate vector and the ratio of the shear stress magnitude to the turbulent kinetic

energy is seen to fall relative to two-dimensional boundary-layer levels. More detailed conclusions can be reached by comparing the present two data sets to previous work in infinite swept flows.

The ratio of the spanwise eddy viscosity component to the streamwise component has a relatively simple behaviour in initially two-dimensional boundary layers when the free-stream flow direction turns monotonically. Comparison of several data sets shows the eddy viscosity ratio decreases with increasing rate of boundary-layer turning. Comparison of the two present data sets show that the ratio is independent of the amount of skewing between the free-stream flow and the wall, at least for rapidly turned cases. This later observation conflicts with the suggestion by Rotta (1979) that the eddy viscosity ratio depends primarily on the amount of skewing through the boundary layer. It should be noted that the above conclusions do not hold in flows approaching separation where the shear stress vector has been found to lead the strain rate vector.

The decline in the shear stress/kinetic energy ratio, A_1 was found to be similar to that observed by Bradshaw & Pontikos (1985) if the last measurement station of their experiment is ignored. Comparing the two cases we see that A_1 decreases more rapidly in a more strongly skewed boundary layer even though the rate of free-stream turning is similar. In contrast to some previous measurements, the drop in A_1 is caused by a very rapid drop in the shear stress magnitude. The turbulent kinetic energy remains relatively constant throughout the boundary-layer distortion.

The simple eddy viscosity model proposed by Rotta (1979) was seen to work well in this simple flow when an appropriate value of T was selected. It seems likely that this T may be selected knowing only the rate of free-stream turning. Unfortunately, the application of Rotta's model is not likely to be straightforward in more complicated flows.

The present experiments do not provide sufficient data to evaluate turbulence closures based on the Reynolds stress transport equations. The apparent non-equilibrium nature of the boundary layer suggests that such a model would be appropriate. However, the triple-product measurements indicate that modelling of turbulent transport of the Reynolds stresses will not be simple.

There are at least two very significant questions that remain unanswered about even simple three-dimensional boundary layers. Perhaps the most important question is: what is the behaviour of the Reynolds stresses in the inner part of the boundary layer (say $0 < y^+ < 50$)? Stress gradients are important in this part of the boundary layer, but there are very few measurements available owing to the constraints of present instrumentation. New measurement techniques should be developed to probe this important region of the flow.

The second question is: why does mean flow three-dimensionality cause such a rapid decrease in the shear stress/kinetic energy ratio? In an early paper, Bradshaw (1971) made the plausible assertion that mean flow three-dimensionality should have little effect on turbulence since the turbulence itself is highly three-dimensional. Experiments have proven this assumption to be incorrect. Bradshaw & Pontikos (1985) later put forth the hypothesis that rapid decreases of shear stress are caused by the sideways tilting of the large eddies away from their preferred orientation. This conclusion is again plausible and is supported by measurements in boundary layers with embedded longitudinal vortices conducted at Stanford and elsewhere.

Another possible explanation is the effect of the crossflow on the near-wall structure of a turbulent boundary layer. The peak in the production of shear stress occurs around $y^+ = 20$ (see Moser & Moin 1987) and is associated with the bursting

event as described by Kim, Kline & Reynolds (1971). The mechanism causing the burst events is still unclear, but it seems obvious that hydrodynamic instability must play a role in the bursting process. Numerous investigators have suggested the presence of streamwise vortices in the near-wall region (see the brief review by Bawirzanski, Randolf & Eckelmann 1987). There is considerable disagreement among various investigators as to the exact nature of the vortices; they may appear either as counter-rotating pairs or as single vortices. But there is general agreement that longitudinal vortices play a major role in the production of turbulence energy and shear stress. Blackwelder (1983) has taken this a step further by suggesting a close analogy between the bursting process and the growth and breakdown of the Görtler instability in laminar flow on a concave wall.

If longitudinal vortices are indeed a key structure in the near-wall regions of turbulent boundary layers, we must be concerned with the interaction of such vortices with a crossflow. In a two-dimensional boundary layer there is no mean longitudinal vorticity and positive and negative vortices must appear with equal probability. However, when a mean crossflow is present there is mean longitudinal vorticity distributed in a sheet. Such a sheet may roll-up into discrete vortices owing to the crossflow instability (cf. Gregory, Stuart & Walker 1955). Longitudinal vortices of opposite sign to the crossflow vorticity may be overwhelmed if the crossflow is large, leaving vortices of only a single sign. Thus, the crossflow may serve to stabilize the turbulence in the near-wall region.

A crude smoke flow visualization was performed, roughly modelling the Case I flow. Smoke was seeped into the sublayer from a spanwise slot allowing observation of the development and breakdown of the sublayer streaks. The sublayer appeared to be more stable when the crossflow angle was large. These experiments, while not definitive, suggest a possibly fruitful avenue for future research. Such research would be simplified if the dynamics of the near-wall turbulence structure in two-dimensional boundary layers were well understood.

We gratefully acknowledge the financial and technical support of the NASA-Ames Research Center (Contract NCC 2-238). The first author was supported by an NSF Graduate Fellowship for the first three years of the study. We have had many helpful discussions with Dr Dennis Johnson of NASA-Ames, Professor P. Bradshaw, Dr V. Baskaran and Dr A. D. Cutler of Imperial College, and our Stanford colleagues Professor J. P. Johnston and W. R. Pauley.

REFERENCES

Abid, R. & Schmitt, R. 1985 An examination of turbulence models for a separating three-dimensional turbulent boundary layer. In *Numerical Methods in Laminar and Turbulent Flows, Swansea, July 9–12, 1985*. Office National D'Etudes et de Recherches Aerospatiales, Chatillon.

Anderson, S. D. & Eaton, J. K. 1987 An experimental investigation of pressure driven three-dimensional turbulent boundary layers. *Rep.* MD 49. Thermosciences Div., Dept. of Mech. Engng, Stanford University.

Baskaran, V. & Bradshaw, P. 1987*a* Experimental investigation of a three-dimensional turbulent shear layer over an 'infinite' swept concave surface. *Proc. 6th Symp. of Turbulent Shear Flows, Toulouse, France.*

Baskaran, V. & Bradshaw, P. 1987*b* Experimental investigation of a three-dimensional boundary layer on an 'infinite' swept concave wing. Imperial College of Science and Tech., Aeronautics Dept., Final Report.

Bawirzanski, E., Randolph, M. & Eckelmann, H. 1987 Direct measurement of streamwise

vorticity fluctuations with a cylinder probe. *Proc. 2nd Intl Symp. on Transport Phenomena in Turbulent Flows, Tokyo,* pp. 605–612.

BEARMAN, P. W. 1971 Corrections for the effect of ambient temperature drift on hot-wire measurements in incompressible flow. *DISA Rep.*, 11, May 1971, pp. 25–30.

BERG, B. VAN DEN 1982 Some notes on three-dimensional turbulent boundary layer data and turbulence modelling. In *Three-Dimensional Turbulent Boundary Layers, IUTAM Symp.* (ed. Fernholz, H. H. & Krause, E.). Springer.

BERG, B. VAN DEN, ELSENAAR, A. & LINDHOUT, J. P. F. 1975 Measurements in an incompressible three-dimensional turbulent boundary layer, under infinite swept wing conditions, and comparison with theory. *J. Fluid Mech.* **70**, 127–148.

BLACKWELDER, R. F. 1983 Analogies between transitional and turbulent boundary layers. *Phys. Fluids* **26**, 2807.

BRADSHAW, P. 1971 Calculation of three-dimensional turbulent boundary layers. *J. Fluid Mech.* **46**, 417–445.

BRADSHAW, P. & PONTIKOS, N. S. 1985 Measurements in the turbulent boundary layer on an 'infinite' swept wing. *J. Fluid Mech.* **159**, 105–130.

BRYER, D. W. & PANKHURST, R. C. 1971 *Pressure-Probe Methods for Determining Wind Speed and Flow Direction.* Her Majesty's Stationary Office, London.

CASTRO, I. P. & CHEUN, B. S. 1982 The measurement of Reynolds stresses with a pulsed-wire anenometer. *J. Fluid Mech.* **118**, 41–58.

DECHOW, R. & FELSCH, K. O. 1977 Measurements of the mean velocity and of the Reynolds stress tensor in a three-dimensinal turbulent boundary layer induced by a cylinder standing on a wall. *Proc. Symp. on Turbulent Shear Flows, April 1977, University Park, Pennsylvania*, vol. I.

DRIVER, D. M. & HEBBAR, S. K. 1985 Experimental study of a three-dimensional, shear-driven turbulent boundary layer using a three-dimensional laser Doppler velocimeter. *AIAA* 85-1610.

EAST, L. F. & SAWYER, W. G. 1979 Measurements of the turbulence ahead of a 45 degree swept step using a double split-film probe. *Royal Aircraft Establishment TR* 79136.

EIBECK, P. A. & EATON, J. K. 1985 An experimental investigation of the heat-transfer effects of a longitudinal vortex embedded in a turbulent boundary layer, *Rep.* MD-48. Thermosciences Div., Stanford University.

ELSENAAR, A. & BOELSMA, S. H. 1974 Measurements of the Reynolds stress tensor in a three-dimensional turbulent boundary layer under infinite swept wing conditions. *NLR TR* 74095 U.

EZEKWE, C. I., PIERCE, F. J. & MCALLISTER, J. E. 1978 Measured Reynolds stress tensors in a three-dimensional turbulent boundary layer. *AIAA J.* **16**, 645–646.

FERNHOLZ, H. H. & VAGT, J. D. 1981 Turbulence measurements in an adverse-pressure-gradient three-dimensional turbulent boundary layer along a circular cylinder. *J. Fluid Mech.* **111**, 233–269.

GREGORY, N., STUART, J. T. & WALKER, W. S. 1955 On the stability of three-dimensional boundary layers with application to the flow due to a rotating disk. *Phil. Trans. R. Soc. Lond.* **248**, 155–199.

HIGUCHI, H. 1983 A miniature, directional surface-fence gage for three-dimensional turbulent boundary layer measurements. *AIAA* 83-1722.

JOHANSSON, A. V. & ALFREDSSON, P. H. 1983 Effects of imperfect spatial resolution on measurements of wall-bounded turbulent shear flows. *J. Fluid Mech.* **137**, 409–421.

JOHNSTON, J. P. 1970 Measurements in a three-dimensional turbulent boundary layer induced by a swept, forward-facing step. *J. Fluid Mech.* **42**, 823–844.

JOHNSTON, J. P. 1976 Experimental studies in three-dimensional boundary layer, *Rep.* MD-34. Thermosciences Div., Stanford University.

KIM, H. T., KLINE, S. J. & REYNOLDS, W. C. 1971 The production of turbulence near a smooth wall in a turbulent boundary layer. *J. Fluid Mech.* **50**, 133–160.

KLEBANOFF, P. S. 1954 Characteristics of turbulence in a boundary layer with zero pressure gradient. *NACA TN*-3178.

MOFFAT, R. J., YAVUZKURT, S. & CRAWFORD, M. D. 1979 Real time measurements of turbulence quantities with a triple wire system. *Flow Dynamics Conf., Marseille, France.*

MOSER, R. D. & MOIN, P. 1987 The effects of curvature in wall-bounded turbulent flows. *J. Fluid Mech.* **175**, 479–510.

MULLER, U. R. 1982 Measurement of the Reynolds stresses and the mean-flow field in a three-dimensional pressure-driven boundary layer. *J. Fluid Mech.* **119**, 121–153.

MULLER, U. R. 1987 Developments in measuring Reynolds stresses. *Perspectives in Turbulence Studies* (ed. H. Meier & P. Bradshaw). Springer.

MURLIS, J., TSAI, H. M. & BRADSHAW, P. 1982 The structure of turbulent boundary layers at low Reynolds numbers. *J. Fluid Mech.* **122**, 13–56.

NAKAYAMA, A. & WESTPHAL, R. V. 1986 The effects of sensor length and spacing on X-wire measurements in a boundary layer. *NASA TM* 88352.

PAULEY, W. R. & EATON, J. K. 1988 The fluid dynamics and heat transfer effects of streamwise vortices embedded in a turbulent boundary layer. *Stanford Univ. Thermosci. Div. Rep.* MD-51. Thermosciences Div., Stanford University.

PIERCE, F. J. & EZEKEWE, C. I. 1976 Measured *uw* stress gradients in a three-dimensional turbulent boundary layer. *Trans. ASME* I: *J. Fluids Engng* **98**, 768–770

PONTIKOS, N. S. 1982 The structure of three-dimensional turbulent boundary layers. Ph.D. thesis, Imperial College, London. (Available on microfiche from Aeronautics Dept.)

PURTELL, L. P., KLEBANOFF, P. S. & BUCKLEY, F. S. 1981 Turbulent boundary layer at low Reynolds number. *Phys. Fluids* **24**, 802–811.

ROTTA, J. C. 1979 A family of turbulence models for three-dimensional boundary layers. In *Turbulent Shear Flows I* (ed. F. Durst, B. E. Launder, F. W. Schmidt & J. H. Whitelaw). Springer.

SAVILL, A. M. 1987 Recent developments in rapid distortion theory. *Ann. Rev. of Fluid Mech.* **19**, 531–575.

TOWNSEND, A. A. 1980 The response of sheared turbulence to additional distortion. *J. Fluid Mech.* **98**, 171–191.

WESTPHAL, R. V. & MEHTA, R. D. 1984 Crossed hot-wire data acquisition and reduction system. *NASA TM* 85871.

YOUNG, A. D. & MAAS, J. N. 1936 The behavior of a Pitot tube in a transverse total pressure gradient. *Aero. Res. Counc. Rep.* 1770.